Axially symmetric relativistic MHD simulations of Pulsar Wind Nebulae in Supernova Remnants

On the origin of torus and jet-like features

Luca Del Zanna[1], Elena Amato[2], Niccolò Bucciantini[1]

[1] Dipartimento di Astronomia e Scienza dello Spazio, Università degli Studi di Firenze, Largo E. Fermi 2, 50125 Firenze, Italy
[2] INAF, Osservatorio Astrofisico di Arcetri, Largo E. Fermi 5, 50125 Firenze, Italy

Abstract. The structure and the evolution of Pulsar Wind Nebulae (PWNe) are studied by means of two-dimensional axisymmetric relativistic magnetohydrodynamic (RMHD) simulations. After the first imaging of the Crab Nebula with *Chandra*, a growing number of objects has been found to show in the X-rays spatial features such as rings and jets, that clearly cannot be accounted for within the standard framework of one-dimensional semi-analytical models. The most promising explanation suggested so far is based on the combined effects of the latitude dependence of the pulsar wind energy flux, shaping the wind termination shock and naturally providing a higher equatorial emission, and of the wind magnetization, likely responsible for the jet collimation by hoop stresses downstream of the shock. This scenario is investigated here by following the evolution of a PWN interacting with the confining Supernova Remnant (SNR), from the free expansion to the beginning of the reverberation phase. Our results confirm the oblate shape of the wind termination shock and the formation of a polar jet with supersonic velocities ($v \approx 0.5 - 0.7c$) for high enough values of the equatorial wind magnetization parameter ($\sigma \gtrsim 0.01$).

Key words. ISM: supernova remnants – ISM: winds and outflows – Pulsars: general – *Magnetohydrodynamics* (MHD) – Shock waves – Relativity

1. Introduction

Pulsar Wind Nebulae (PWNe, or plerions) arise from the confinement of pulsar winds by the surrounding medium, usually an expanding Supernova Remnant (SNR). The relativistic magnetized pulsar wind is slowed down to non-relativistic velocities at a termination shock, where the magnetic field is compressed and the bulk energy of the outflow is converted into heat and acceleration of particles. These then give rise to the synchrotron and Inverse Compton emission observed from plerions in a very wide range of frequencies, extending from radio wavelengths to X-rays and even γ-rays.

The best studied plerion is the Crab Nebula, whose emission has been extensively investigated in all frequency bands and for which most models have been proposed. New light on the spatial structure of the Crab Nebula emission at high frequencies has been shed by observations made with the *Chandra* X-ray satellite (Weisskopf et al. 2000), which, thanks to the unprecedented spatial resolution, has revealed a number of intriguing features in the inner part of the nebula (see also Hester et al. 1995, 2002). The new details highlighted strengthen the view of the Crab Nebula as an axisymmetric object. In what

is thought to be the equatorial plane of the pulsar rotation, *Chandra* observations show the presence of a bright ring of emission, lying at a much closer distance to the pulsar than the already identified X-ray torus (e.g. Hester et al. 1995). The most puzzling discovery, however, is probably the presence of two opposite jet-like features oriented along an axis perpendicular to the plane of the torus and emerging from the very close vicinity of the pulsar. Similar features have been observed also in a number of other objects, namely around the Vela pulsar (Helfand et al. 2001; Pavlov et al. 2003), PSR 1509-58 (Gaensler et al. 2002) and in the supernova remnants G0.9+01 (Gaensler et al. 2001) and G54.1+0.3 (Lu et al. 2002).

While the presence of a X-ray bright torus may be at least qualitatively explained within the framework of standard 1-D RMHD models (Kennel & Coroniti 1984, KC84 hereafter; Emmering & Chevalier 1987), if we further assume that either the energy flux emerging from the pulsar or the termination shock dissipation efficiency is higher at low latitudes around the equator, the presence of jets that seem to emanate directly from the pulsar poses severe theoretical problems in its interpretation (Lyubarsky & Eichler 2001), given the difficulties at explaining self-collimation of ultra-relativistic flows. A recent suggestion for an answer to this puzzle (Bogovalov & Khangoulian 2002a, 2002b; Lyubarsky 2002) is that the jets

are actually originating downstream of the pulsar wind termination shock, where the flow is only mildly or non-relativistic. If this is the case, the fact that they are observed starting from a much closer distance from the pulsar than where the shock in the equatorial plane is thought to be, has to be interpreted assuming that the given degree of anisotropy in the energy flow from the pulsar also causes the shock front to be highly non-spherical in shape, much closer to the pulsar along the rotation axis than in the equatorial plane. Moreover, even if the pulsar wind is weakly magnetized just upstream of the termination shock, the magnetic field inside the plerion can become as high as to reach equipartition. Therefore, collimation of the downstream flow may be easily achieved there by magnetic hoop stresses (Lyubarsky 2002; Khangoulian & Bogovalov 2003), resulting in plasma compression toward the axis and eventually in a polar jet-like outflow.

Thanks to the recent progress in numerical relativistic fluid dynamics and MHD (see Del Zanna & Bucciantini 2002; Del Zanna et al. 2003, and references therein), we are now able to start a more quantitative investigation of this problem by means of computer simulations. Our aim is to clarify whether a given latitude dependence of the pulsar wind energy flux may actually explain the jet-torus morphology observed at X-ray frequencies for the Crab Nebula and other plerions, and, if this is the case, what are the conclusions that one may infer on the structure and magnetization of the unshocked pulsar wind. Here we present the results of a first series of long-term 2-D axisymmetric RMHD simulations, from which some general conclusions on the physical mechanisms at work and useful scalings may already be derived (see Amato et al. 2003 for preliminary results). A similar numerical investigation has been recently carried out (Komissarov & Lyubarsky 2003, KL03 hereafter), confirming the basic physical picture as viable for explaining the main observational features, as strongly suggested also by the close resemblance, at least at a qualitative level, between the map of simulated emission and *Chandra* images of the Crab Nebula.

The paper structure is as follows. In Sect. 2 the pulsar wind model adopted at large distances from the light cylinder is sketched. In Sect. 3 the numerical details of the simulations and the initial conditions are reported. Sect. 4 deals with the results of the simulations, split in three sub-sections for convenience. Finally the results are summarized in Sect. 5, where conclusions are drawn for this preliminary work.

2. Pulsar wind model and pre-shock conditions

The key point of all attempts at interpreting the torus and the jet-like features observed in plerions as arising post-shock is that the energy flux in the unshocked pulsar wind should depend on latitude as $\sin^2 \theta$ (Bogovalov & Khangoulian 2002a; Lyubarsky 2002). This angular dependence is related to the structure of the residual purely toroidal magnetic field, which, far enough from the pulsar, is expected to depend on the polar angle as $\sin \theta$ (*split monopole* models: e.g. Michel 1973; Bogovalov 1999). We further assume that along the way to the termination shock the residual Poynting energy flux is almost entirely converted into particle energy flux, as in clas-

sic models, preserving the overall angular dependence. We do not address here the fundamental problem of how the acceleration of the outflow and the conversion of magnetic to particle energy may occur, the so-called σ paradox: see however Vlahakis (2004) and references therein for self-similar 2-D relativistic MHD models, though many other mechanisms involving waves, reconnection or kinetic plasma processes have been proposed (see e.g. Arons 2003 for a review and references therein). Therefore, in the present work we will consider as an initial condition an axisymmetric cold ($p \ll \rho c^2$) relativistically expanding pulsar wind ($v_r \approx c$), with a small ratio between electromagnetic and particle energy fluxes just upstream of the termination shock, thus extending the standard KC84 picture to 2-D.

Following the previous analytical studies cited above, let us then introduce the latitude dependence of the energy flux from the pulsar as a dependence on θ of the wind Lorentz factor γ, namely:

$$\gamma(\theta) = \gamma_0[\alpha + (1 - \alpha) \sin^2 \theta], \tag{1}$$

where the subscript 0 indicates quantities in the equatorial plane, and $\alpha \leq 1$ is a parameter controlling the ratio between the Lorentz factor at the pole and that at the equator. We then assume the streamlines to be radial upstream of the shock and the mass flux to be isotropic (Bogovalov & Khangoulian 2002a):

$$\rho(r, \theta) = \rho_0 \left(\frac{r_0}{r}\right)^2 \frac{\gamma_0}{\gamma(\theta)}, \tag{2}$$

with r_0 the (arbitrary) distance from the pulsar on the equatorial plane at which the value ρ_0 is assigned. As it was shown in the above cited work, these assumptions, in the case of a weakly magnetized outflow, naturally give rise to an oblate shape of the termination shock front, and imply the existence, around the axis, of a colder, denser sector of the downstream plasma.

As anticipated, the toroidal magnetic field $B \equiv B_\phi$ is defined as

$$B(r, \theta) = B_0 \frac{r_0}{r} \sin \theta. \tag{3}$$

It is important to notice that the adopted pulsar wind model leads to a ratio between Poynting and kinetic energy fluxes that does depend on latitude but not on distance from the pulsar. Therefore, it is convenient to take its equatorial (maximum) value σ as the independent parameter controlling the wind magnetization (thus the same quantity used by KC84) and let B_0 derive from it as $B_0 = (4\pi\rho_0 c^2 \gamma_0^2 \sigma)^{1/2}$. The total wind energy flux $F \simeq c(\rho c^2 \gamma^2 + B^2/4\pi)$ may then be written as

$$F(r, \theta) = \rho_0 c^3 \gamma_0^2 \left(\frac{r_0}{r}\right)^2 [\alpha + (1 - \alpha + \sigma) \sin^2 \theta], \tag{4}$$

and the wind anisotropy in energy flux is, at any distance, given by the value $F(r, 0)/F(r, \pi/2) = \alpha/(1 + \sigma)$. Finally, the value of ρ_0 is determined from the total pulsar spin-down luminosity, supposed to be constant in time for simplicity (see Bucciantini et al. 2003, 2004 for long-term spherically symmetric simulations in the case of a decaying luminosity in time).

A similar wind model and pre-shock conditions were adopted by KL03, though the assumed mass flux was not isotropic but had the same latitude dependence as the energy flux ($\gamma = \gamma_0 = 10$ and $F(\theta) \sim \sin \theta^2$), and the toroidal magnetic field a different shape: while in our case we take a field with its maximum at the equator, allowing direct comparison with standard 1-D models and the usual definition of σ, in the cited work the field reaches the maximum at intermediate latitudes and then goes smoothly to zero at the equator (see Sect. 4.3 for a detailed discussion and comparison). In spite of these differences, the overall latitude dependence of the wind energy flux, which is the quantity that really matters in shaping the termination shock, is in both cases the one predicted in the cited analytical studies.

3. Simulation setup

3.1. Numerical settings

The problem of the interaction of the pulsar wind sketched above with the surrounding medium is here addressed numerically by performing 2-D axisymmetric simulations. The numerical tool employed is the shock-capturing code for relativistic MHD developed by Del Zanna et al. (2002, 2003). The scheme is particularly simple and efficient, since complex Riemann solvers based on characteristic waves are avoided in favor of central-type component-wise techniques: the solver is defined by the two fastest local magnetosonic speeds and spatial reconstruction at cell boundaries is achieved by using ENO-type interpolating polynomials. However, due to the extremely small time-steps required in the present simulations and because of the high Lorentz factors involved (numerical oscillations are most dangerous in the ultra-relativistic regime), third order reconstruction is avoided and simpler second order limited reconstruction is employed. Time integration is achieved by means of a two-stage Runge-Kutta TVD algorithm, using a CFL number of 0.5.

The spatial grid is defined by spherical coordinates with 400 cells in the radial direction and 100 cells in the polar angle θ. The physical domain of the simulation ranges in radius from $r_{\min} = 0.05$ to $r_{\max} = 20$ light-years (we assume a unit length $r_0 = 1$ light-year, from now on all lengths will be expressed in light-years, time intervals in years and velocities in units of c, if not explicitly stated otherwise), and a logarithmic stretching ($dr \sim r$) is imposed to better resolve the inner region. Note that, in order to resolve within a few computational cells the contact discontinuity between the lighter relativistic plasma and the heavy SNR ejecta (typical jumps of order 10^6, see below), artificial compression is required, especially at large radii where resolution is necessarily lower. This may in principle amplify spurious noise above the threshold of dissipation by numerical viscosity, thus producing unphysical results or even code crashing. We have verified that the chosen grid and scheme settings are a good compromise between resolution and stability.

Stationary input for all quantities is imposed at $r_{\min}$, where the super-Alfvénic wind is blowing from, while zeroth order extrapolation is assumed at the outer boundary. The domain in θ is the first quadrant $(0, \pi/2)$, with reflecting conditions for v_θ and B at the polar axis to enforce axisymmetry, and on v_θ alone on the equatorial plane. Note that all quantities are defined in our code at cell centers, which never coincide with the symmetry axis $\theta = 0$ where singularities may occur. By doing so, the ghost cells technique is well suited for all non-cartesian problems and we never find carbuncle-like effects (see the jet propagation tests in cylindrical geometry in Del Zanna & Bucciantini 2002; Del Zanna et al. 2003).

Notice that under these particular settings, only 5 (out of 8) RMHD variables need to be evolved in time. Moreover, the magnetic field is forced to be in the azimuthal direction alone, and thus always perpendicular to the velocity vector, by the assumed geometrical symmetries. In this case, all the specific methods to treat the divergence-free constraint are obviously of no use, and the magnetic field may be evolved as an ordinary fluid variable. Other important simplifications occur in the algorithm for calculating the local magnetosonic speeds and in that for deriving the primitive variables from the set of conservative variables (see Del Zanna et al. 2003). In order to speed up calculations, the pre-shock quantities are not updated in time and the global time-step is defined at the inner termination shock radius (on the axis), which is moving outward thus having the effect of accelerating the simulation.

3.2. Initial conditions and simulation parameters

The initial conditions are given as follows. The pulsar wind, modeled as in Sect. 2, is set up within an arbitrary radius of 0.2. Once the two free parameters α and σ are provided, the wind is uniquely determined by the equatorial Lorentz factor γ_0 and total wind luminosity L_0. Appropriate values of the above parameters come by fits of the high-energy emission (for the Crab Nebula) based on spherically symmetric MHD (KC84) and kinetic (Gallant & Arons 1994) models of the wind-nebula interaction, namely $\gamma_0 \gtrsim 10^6$ and $L_0 \simeq 5 \times 10^{38}$erg s^{-1}.

From a numerical point of view, however, such a high Lorentz factor is well beyond the capabilities of existing relativistic MHD codes. Here we assume $\gamma_0 = 100$ (notice that ours are the multidimensional RMHD simulations with the highest Lorentz factor available in the literature so far), and an *averaged* wind luminosity of 5×10^{39}erg s^{-1}, in order to speed up the evolution. The resulting rest mass densities will be of course unrealistically high, since we basically have $\rho_0 \gamma_0^2 = $ const. We deem that this should not a problem even in multidimensional flows, provided $\gamma \gg 1$ in the wind region at all latitudes (as in our case). This property has been nicely demonstrated in 1-D by KC84, where there is no explicit dependence on γ and ρ taken separately, while all quantities depend on the wind luminosity and on the magnetization parameter σ. In the present 2-D case, even if the termination shock is not circular in shape (thus the wind is not always normal to it and KC84 analysis do not apply at all latitudes), we still find that the exact value of γ_0 does not make any difference in the nebular flow, provided all other parameters (except obviously ρ_0) are kept the same. In particular we have performed runs with lower values of the equatorial Lorentz factor, down to $\gamma_0 = 20$ (here with a small

wind anisotropy, $\alpha = 0.5$, to preserve the condition $\gamma \gg 1$ at the poles too), and we did not find appreciable differences in the results.

In all simulations we assume an anisotropy parameter of $\alpha = 0.1$, thus the energy flux along the polar axis will be ten times less than at the equator, while density will be ten times greater. We decided not to choose smaller values of α since we wanted to be sure that during the evolution the termination shock (TS hereafter) would eventually move away from the inner boundary at all latitudes, otherwise outflow conditions are not appropriate and may lead to unphysical situations, typically near the polar axis. The magnetization parameter σ is instead varied in the different simulations, from 0.003 up to 0.1.

Around the pulsar wind region, the (spherical) expansion of the cold, unmagnetized supernova (SN) ejecta is simulated by setting up a region of high constant density with a radially increasing velocity profile $v = v_{ej}r/r_{ej}$, appropriate for a self-similar expansion. Here we take $r_{ej} = r_0 = 1$, while ρ_{ej} and v_{ej} are respectively determined by imposing

$$M_{ej} = \int_0^{r_{ej}} \rho_{ej} 4\pi r^2 dr, \tag{5}$$

where we take $M_{ej} = 3M_\odot = 6 \times 10^{33}$g, and

$$E_{ej} = \int_0^{r_{ej}} \frac{1}{2}\rho_{ej} v^2 4\pi r^2 dr, \tag{6}$$

with $E_{ej} = 10^{51}$erg. The velocity at the outer boundary of the ejecta is then $v_{ej} \approx 7500$ km s^{-1}, corresponding to an age of the SNR of $r_{ej}/v_{ej} \approx 40$ years, while the velocity at the contact discontinuity between the ejecta and the relativistic material (CD hereafter) is $v_{ej} \approx 1500$ km s^{-1}. Farther out, between r_{ej} and r_{max}, ISM conditions are imposed, that is a uniform, static, unmagnetized background with $\rho_{ISM} = 10^{-24}$g cm^{-3} $p_{ISM} \approx 10^{-12}$dyne cm^{-2}. For similar settings see van der Swaluw et al. (2001), Blondin et al. (2001), Bucciantini et al. (2003; 2004).

Finally, for simplicity we adopt here a uniform value of 4/3 for the adiabatic index, appropriate for a relativistic plasma. Radially symmetric simulations of the PWN - SNR interaction with a variable adiabatic index (5/3 in the ejecta and ISM regions) were performed by Bucciantini et al. (2003), to which we refer for a discussion of the complications implied.

Note that in KL03 the ISM is absent and ejecta expanding with a velocity of 5000 km s^{-1} are set everywhere beyond the wind region. This allows to speed up the evolution of the TS, though important processes due to the interaction with the external ISM (namely the reverberation phase, see below) are completely neglected.

4. Simulation results and discussion

4.1. Overall PWN structure and evolution: comparison with analytical models

Before studying the formation of the peculiar jet-torus structure seen in *Chandra* images, let us investigate the overall plerion properties and its evolution in time, comparing the results with analytical models, whenever possible.
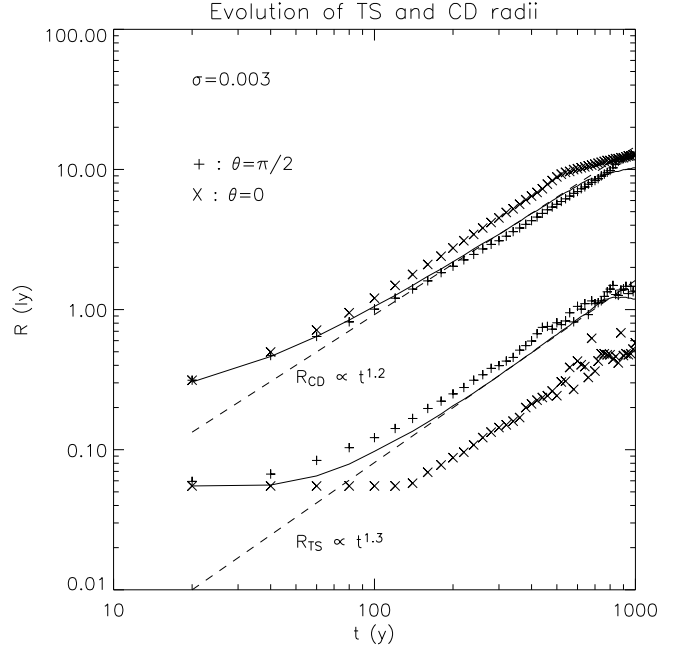

Fig. 1. The time evolution of the PWN boundaries, the TS and CD radii, for $\theta = \pi/2$ and $\theta = 0$ (symbols as indicated on the plot), in the $\sigma = 0.003$ case. The 2-D results are compared with a spherically symmetric case (solid curves) set up with the parameters corresponding to the equatorial outflow of the 2-D case. The self-similar 1-D hydro solution (dashed curves) is also shown for comparison.

The PWN evolution is followed up to $t = 1000$ for four cases with different magnetization: $\sigma = 0.003$, $\sigma = 0.01$, $\sigma = 0.03$, and $\sigma = 0.1$. After a short (a few years) transient stage during which, after the nebula is first formed, the reverse shock propagates backward, both the wind termination shock and the contact discontinuity (the latter separates the nebula from the swept up shell of ejecta) move outward. In Fig. 1 the evolution of the PWN boundaries for $\theta = \pi/2$ and $\theta = 0$ is plotted against time, in the $\sigma = 0.003$ case. For a comparison, also the corresponding 1-D spherically symmetric evolution is shown, together with the fits expected for (hydrodynamical) self-similar models of PWN interacting with freely expanding SN ejecta (see Bucciantini et al. 2004, and references therein). At later times ($t \approx 500$ in this case) the expected self-similar expansion is slowed down because of the interaction with the reverse shock produced by the motion of the SNR in the surrounding ISM. This is the beginning of the so called *reverberation* phase (see Bucciantini et al. 2003), here occurring rather early because of the high spin-down luminosity adopted.

As expected, the PWN inner boundary (the termination shock, TS hereafter) is farther from the pulsar at the equator than at the pole, while the opposite occurs at the outer boundary (the contact discontinuity, CD hereafter). The former effect is due to the assumed wind energy flux anisotropy which produces the oblate shape of the TS. The latter effect is due, instead, to the pinching by the PWN magnetic field (Begelman & Li 1992; van der Swaluw 2003). Similar results are found also for more magnetized winds, although for higher values
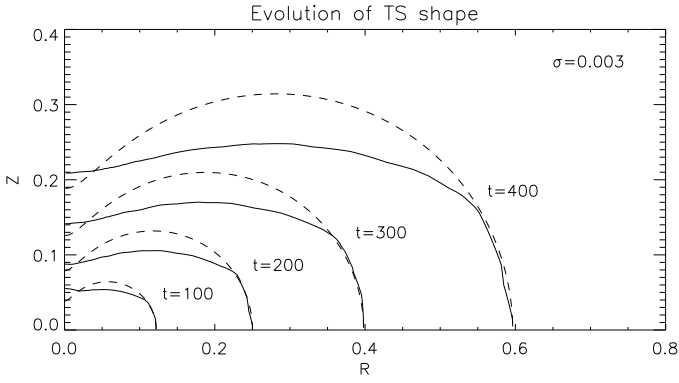
Fig. 2. The time evolution of the TS radius in the case $\sigma = 0.003$, in the cylindrical coordinates R and Z (solid line). Together with the shock shape resulting from the simulation, the expression in Eq. 8 is plotted for comparison as a dashed curve. Before reverberation starts ($t \approx 500$), the ratio between the polar and equatorial radii is also well reproduced.
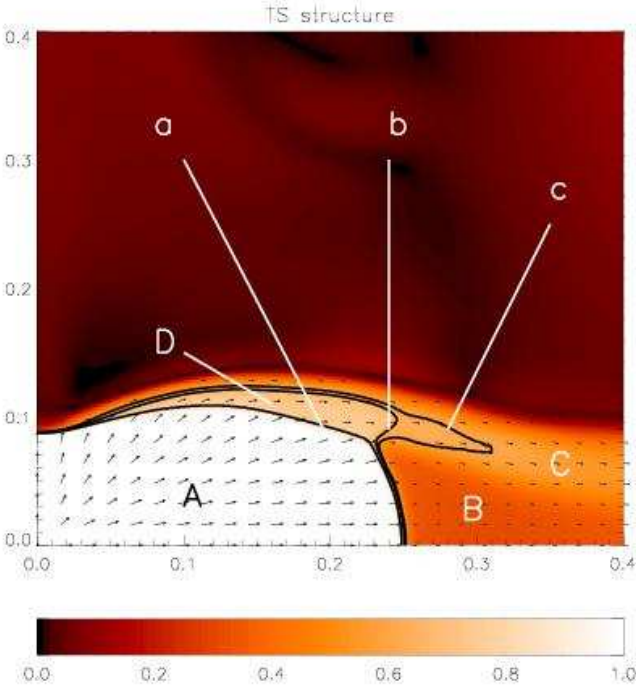

Fig. 3. The flow structure around the TS. The background 2-D gray-scale plot refers to the velocity magnitude. The arrows indicate the streamlines. Labels refer to: A) ultrarelativistic wind region; B) subsonic equatorial outflow; C) equatorial supersonic funnel; D) super-fastmagnetosonic shocked outflow; a) termination shock front; b) *rim shock*; c) fastmagnetosonic surface.

Fig. 4. The time evolution of the PWN elongation, that is the ratio of the CD radii at the pole and at the equator, for the various values of the wind magnetization parameter. The elongation starts decreasing in time when the CD reaches the SNR-ISM reverse shock along the polar axis.

Let us discuss in greater detail the above results. The time evolution of the TS shape is shown in Fig. 2 for the case $\sigma = 0.003$. If the downstream total pressure were constant, the TS profile at a given time would be simply defined by the condition

$$F(r, \theta) \cos^2 \delta = \text{const},\qquad(7)$$

where δ is the angle between the shock normal and the radial direction. We have verified that the approximation of constant downstream pressure is reasonable only within an angle ϵ around the equator, with $\epsilon \sim 20°$ for $\alpha = 0.1$ as in the present simulations. At these latitudes one also has $\delta \approx 0$, leading to the following approximate expression for the TS profile:

$$R_{TS}(\theta) \simeq R_{TS}(\pi/2) \left[\frac{\alpha + (1 - \alpha + \sigma) \sin^2(\theta)}{1 + \sigma} \right]^{1/2}.\qquad(8)$$

The latter expression is plotted against the numerical solution for the shock front in Fig. 2 for each time. The deviations from the predicted shape at intermediate latitudes are mostly due to pressure variations in the post-shock region: the pressure constancy is verified only within an order of magnitude due to the magnetic pinching effect and the presence of supersonic flows. Due to this fact, no improvement is observed if one plots the exact solution of Eq. 7 instead of the expression in Eq. 8. Another thing to notice from the profiles shown in Fig. 2 is that the evolution of the shock shape appears to be self-similar. We have checked that this result holds also for all the other values of σ considered (as long as the PWN evolution remains in the free expansion stage).

The detailed structure of the flow in the vicinities of the TS is shown in Fig. 3, where its complexity is apparent. Here we show the different regimes of the post-shock flow: in region D, due to the obliquity of the TS, the speed remains super-fastmagnetosonic, until the plasma crosses the *rim shock* (labeled in figure as b: see also KL03), and it is finally slowed

of σ the TS evolution is slower and its expansion can begin only when 2-D effects (vortexes) remove the $\sigma < v_{CD}/c$ constraint for quasi-stationary radial MHD flows (KC84; see also Bucciantini et al. 2004 for discussions about this constraint).
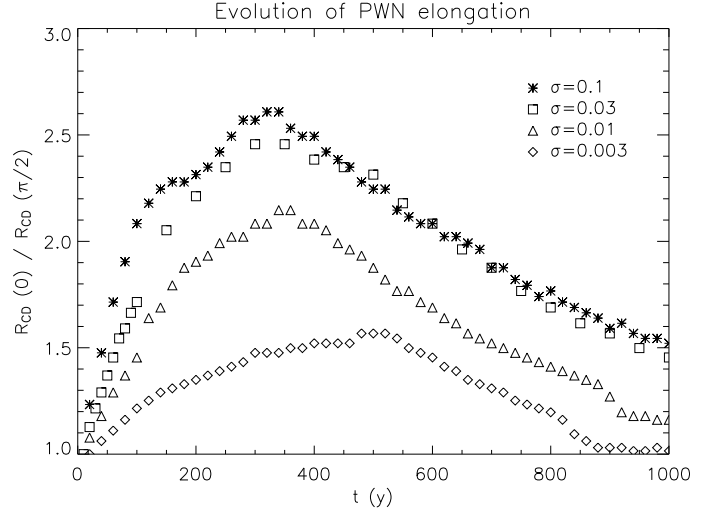
down to sub-fastmagnetosonic, yet still supersonic, speeds in the funnel C. The TS front between the equator and the rim shock latitude ϵ (see above) is almost perpendicular to the wind (here is where Eq. (8) is a good approximation), so that the latter is directly slowed down to subsonic speeds (region B).

In Fig. 4 the PWN elongation, defined as $R_{CD}(0)/R_{CD}(\pi/2)$, is shown as a function of time for all the different values of the wind magnetization, thus extending the analysis by van der Swaluw (2003) to the relativistic case and to higher magnetizations. We confirm the result that the elongation increases with time and with σ. The growth with time is limited to the free expansion phase, before the interaction with the reverse shock from the ISM. When this interaction starts, it has two consequences: the reduction in time of the elongation, eventually toward unity, and the saturation of the elongation increase with σ. We reiterate that this interaction begins early in time in our simulations because of the high spin-down luminosity assumed.

The situation for the low σ case is displayed in Fig. 5, where 2-D plots of various quantities are shown for $t = 400$ and $t = 1000$ (the magnetization is defined here as the ratio between the magnetic and thermal pressure).

At early times the PWN is clearly elongated along the symmetry axis, since from the density and pressure plots we can see that the interaction with the outer shell (SNR blast wave and reverse shock) has not started yet, except for the pole where it is just beginning. Notice that not only the elongation, but also the expected shape for a PWN expanding in fast moving SN ejecta is, at least qualitatively, reproduced (see Fig. 2, case c, in the paper by Begelman & Li 1992). The other prediction in the cited work, namely the dependence of the total pressure on the cylindrical radius alone inside the PWN, is reproduced quite well, as the corresponding contours are nearly parallel to the vertical axis. As mentioned previously, it is only in the close vicinities of the TS that major deviations, including discontinuities, occur. Notice, however, that such overall pressure distribution is supposed to hold only approximately, since the assumed wind energy flux is strongly anisotropic and vortexes of non-negligible speed may form. The presence of these vortexes is also the cause of a dragging of high density material from the ejecta, that starts close to the pole and later extends to the entire nebula (see the first plot in Fig. 5). However, this fact does not seem to affect the overall dynamics, at least for low σ values. From the third plot we can have an estimate of the relative importance of magnetic and thermal effects, whose ratio increases with the cylindrical radius, again as expected.

At much later times, namely $t = 1000$, the PWN has expanded so much that the interaction with the reverse shock in the ejecta occurs at all latitudes. The dependence of the thermal and magnetic pressures on the cylindrical radius still holds approximately, but the shape of the PWN is no more elongated, since in spite of the pinching effect, which is still at work, the external boundaries are now defined by the spherical SNR shell. Due to the high value of the sound speed (actually fast magnetosonic speed) inside the PWN, waves and disturbances created at the interaction interface between the PWN and the SNR are rapidly transmitted and distributed through-

out the whole PWN, back to the TS that changes in shape and slows down its evolution (see Fig. 1).

In the above discussion reference was made to the simulation with $\alpha = 0.1$ and $\sigma = 0.003$ (the latter is the standard value deduced for the Crab Nebula from 1-D radial models, see KC84). Let us now briefly discuss how the above results depend on these parameters. The energy flux anisotropy is crucial for determining the TS shape, see Fig. 2 and Eq. (8), though runs with different values of α show that the overall morphology and evolution of the PWN are basically unchanged. More important is the value of the wind magnetization parameter σ, which determines the PWN elongation and, as a side effect, also the time at which the interaction with the reverse shock begins (see Fig. 4). In the following section we will discuss in greater detail the role played by the magnetization in the physics of the PWN and in particular in the formation of the polar jets.

4.2. Formation of jet-like features

Let us now investigate how the flow pattern inside the PWN is affected by the nebula magnetization. In Fig. 6 we show the speed magnitude and the streamlines for increasing values of σ, namely 0.003, 0.01 and 0.03, at the same time $t = 400$. The jet is basically absent in the low magnetization case, where only a subsonic flow ($v \lesssim 0.1$) is observed along the polar axis. In the intermediate case the polar outflow starts to be more collimated and its speed increases to supersonic velocities. Finally, in the high magnetization case, a strong, well collimated jet is clearly apparent. It has supersonic speed reaching values as high as $v \approx 0.7 - 0.8$.

The presence of the polar jet seems to be directly correlated to the flow pattern in the rest of the nebula. In the first two cases an equatorial flow with speeds $v \approx 0.5$ is present, together with large scale vortexes at higher latitudes. The fast equatorial flow is entirely due to 2-D effects, since the streamlines bend toward the equator after crossing the toroidal TS (Bogovalov & Khangoulian 2002a). The vortexes occur when this equatorial flow hits the expanding CD boundary and a circulating back-flow is created. This pattern is present in hydro simulations as well with the unmagnetized case being very similar to the $\sigma = 0.003$ case in Fig. 6. With increasing value of the wind magnetization the equatorial outflow, for this choice of Poynting flux dependence on latitude, is progressively suppressed. For $\sigma = 0.03$ the flow in the equatorial plane is limited to the close vicinities of the TS. A situation very similar to the latter is found in the highest magnetization case we considered, $\sigma = 0.1$, which is not displayed in the figure.

As mentioned above, a polar subsonic outflow is present even in the hydro simulations. The reason for this is that large scale vortexes eventually reach the high latitude regions near the axis, compress the plasma there and drive a polar flow. In addition to this process, as the σ of the wind increases, the magnetic hoop stresses cause the formation of the jet-like feature with super-fast-magnetosonic speeds: the tension of the toroidal magnetic field, amplified downstream of the TS, diverts the equatorial flow toward the polar axis, well before the
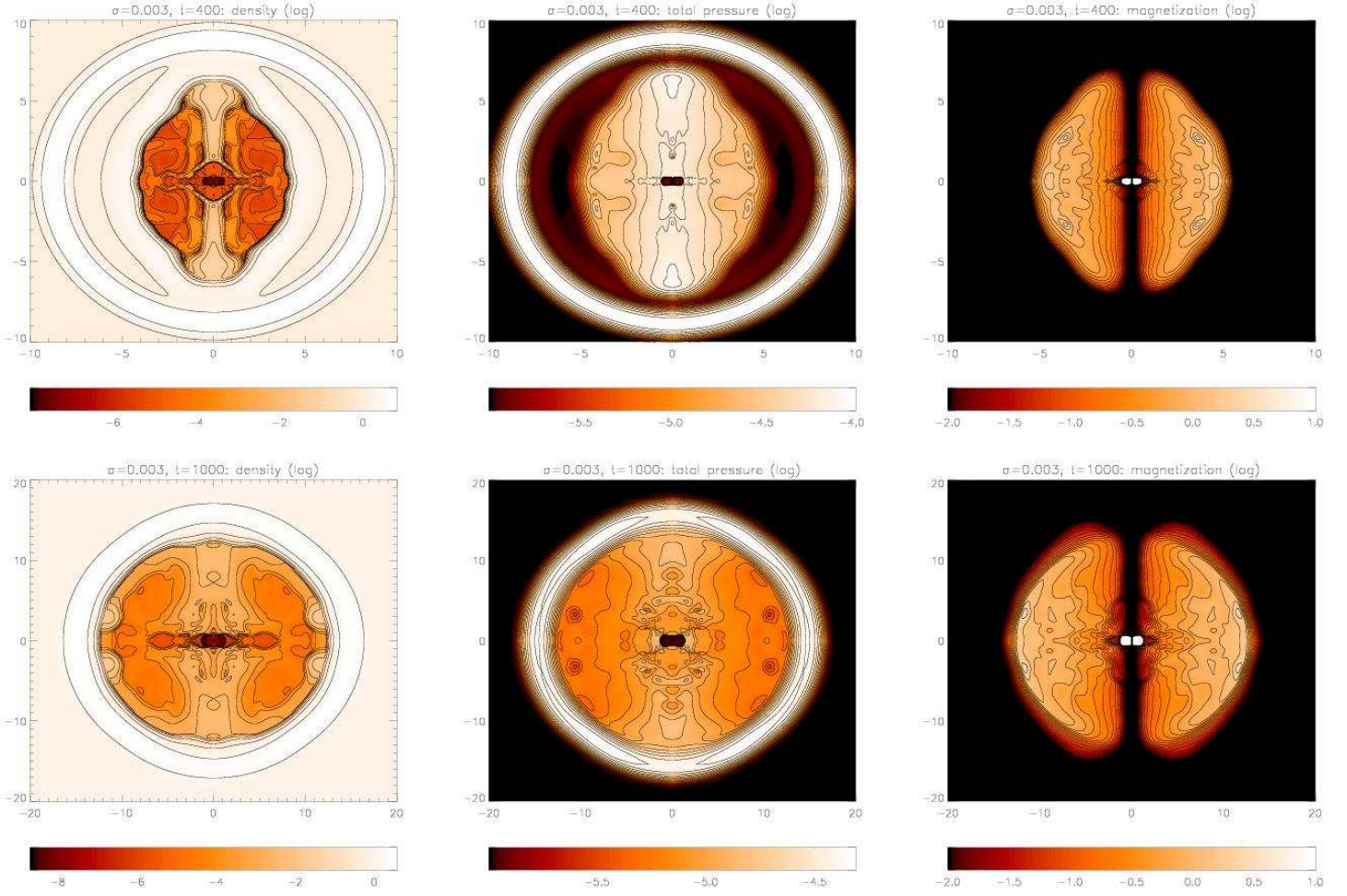
Fig. 5. 2-D gray-scale and contour plots of the density, total pressure and magnetization (ratio of magnetic to thermal pressure), in logarithmic scale. The fields are shown for the case $\sigma = 0.003$, at time $t = 400$ (upper row) and $t = 1000$ (lower row, notice that the displayed regions are different).

large scale vortexes due to interaction with the CD outer boundary are even formed.

This mechanism has been theoretically predicted by Lyubarsky (2002), analysed by Khangoulian & Bogovalov (2003) and finally confirmed numerically by KL03. In particular, in the last cited work the authors show that significant polar velocities are found when the effective wind magnetization parameter is $\sigma \approx 0.01$ or higher. In spite of the different settings (especially the shape of the pulsar wind magnetic field: see next section) it is interesting to notice that we basically confirm here a similar value for the threshold between cases in which the polar outflow is well developed and supersonic and cases in which it is not.

Let us consider the case $\sigma = 0.03$ and follow more closely what happens in the inner regions around the TS. In Fig. 7 we plot the velocity field, magnetization and density at two different times: $t = 200$ (upper row) and $t = 300$ (lower row). By following the streamlines in the first panel we can understand the launching mechanism. Due to the highly non-spherical shape of the termination shock, narrow channels of supersonic post-shock flow form along its boundary, and then

converge toward the equatorial plane, where they merge in the high speed ($v \approx 0.7$) equatorial beams present also in low-σ and hydro simulations. However, this flow is no longer able to reach the outer boundary of the PWN. After a few TS radii, the hoop stresses due to the high magnetization in the inner part of the nebula (even beyond equipartition: see the second plot) are so strong as to inhibit this flow completely, thus a back-flow and vortexes form there. When this back-flow reaches the polar axis, part of it directly escapes along the axis, another part of it circulates back into the equatorial flow, and yet another part heats up the plasma in the cusp region just on top of the TS, driving again a polar outflow. The final result is then the complete suppression of the equatorial flow at a small radius and the formation of a high velocity ($v \approx 0.7$) polar jet.

At $t = 300$, additional effects have occurred. The TS has moved farther out, while the equatorial outflow region has started shrinking, with the result of enhancing the jet driving mechanism even more. The reason for this unexpected behavior can be appreciated by the density maps. Fingers of cold, dense material protruding from the ejecta through the CD crunch the highly magnetized region of the PWN. Rather than the result
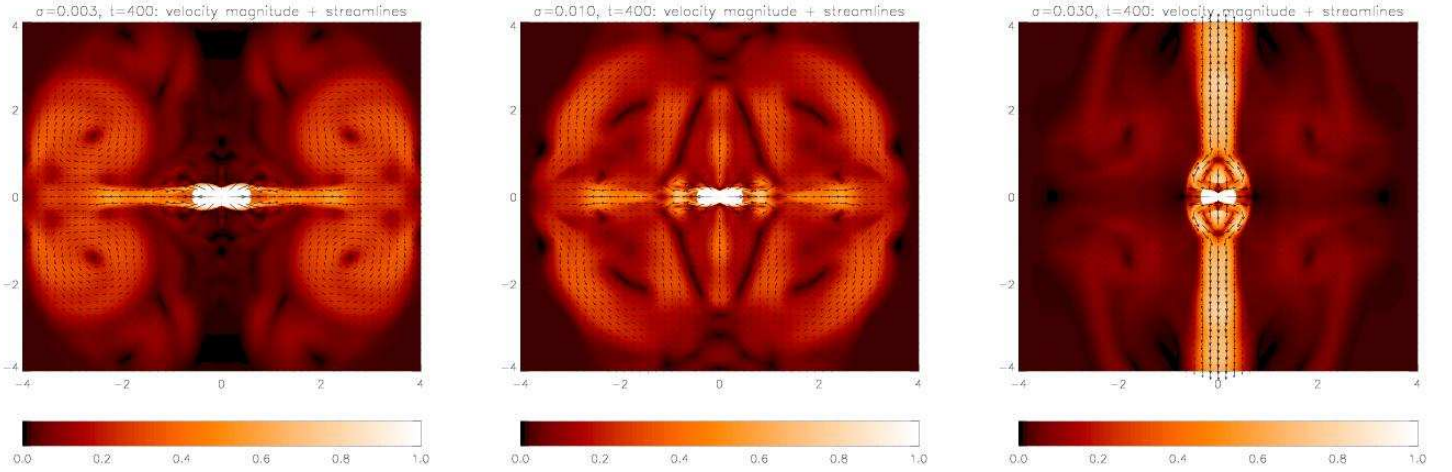
Fig. 6. Flow magnitude (gray scale images) and streamlines at time $t = 400$ for three values of the wind magnetization parameter σ. The jet starts to form for $\sigma = 0.01$ and it is very well developed for higher values.

of some instability (Rayleigh-Taylor and/or Kelvin-Helmoltz) this density enhancement coming from the external equatorial regions is rather due to the large scale circulation induced by the jet interaction with the slowly expanding ejecta. The polar flow is suddenly diverted along the CD all the way down to the equatorial region, where it goes back toward the center eventually dragging with it the dense material from the ejecta (faint vortexes with $v = 0.1 - 0.2$ are present also in the last plot of Fig. 6).

While the inner nebula region is very well resolved, due to the logarithmic radial stretching of the computational grid, one may wonder whether the outer large scale vortexes and the dragging of the dense material from the CD are indeed numerically converged features, since resolution becomes correspondingly poor at large distances. In order to check this point we have performed a long-term run with double resolution (800×200). The results show that the overall structure is maintained, especially in the inner region (corresponding to the X-ray most luminous region). However, the higher resolution allows the development of smaller scale vortexes and instabilities, so that the dragging is more efficient and saturation occurs earlier, although the global behaviour is preserved.

To summarize, the pulsar wind anisotropy is responsible for the non-spherical shape of the TS, which makes the material flow along its boundary to form eventually the high velocity outflow in the equatorial plane. If the wind magnetization parameter σ is high enough, equipartition is reached in the PWN equatorial region very near the TS and this flow can be completely suppressed by hoop stresses and diverted toward the polar axis, where part of it will drive the super-fastmagnetosonic jet. When this polar outflow starts interacting with the slowly expanding ejecta, the material escapes along the CD down to the equator, where high density cool plasma is dragged by the large scale vortexes toward the center causing the crushing of the inner part of the nebula.

4.3. Dependence on the wind magnetic field shape

When defining the wind properties we have assumed a $\sin\theta$ latitude dependence for the toroidal field, thus the magnetization is taken to be highest at the equator. However, since the toroidal magnetic field is the residual of the global field at large distances from the pulsar, around the equatorial plane it is bound to change sign. Even assuming the simplest case, that is the split monopole model (Michel 1973) for a perfectly aligned magnetic rotator, at large enough distances from the light cylinder $r \gg c/\Omega$ (Ω is the pulsar angular velocity) the toroidal field eventually becomes

$$B_\phi = \frac{\Omega r \sin\theta}{v_r} B_r, \qquad (9)$$

and since B_r changes sign at $\theta = \pi/2$ also B_ϕ is bound to do so. If the pulsar dipolar field is not exactly aligned with the rotation axis, the so-called *striped wind* on the equator will present a sequence of fieldlines of alternating sign. If magnetic dissipation (reconnection) is efficient, the effective toroidal field at large distances will be approximately zero below a certain small angle (depending on the obliquity of the rotator) around the equator (e.g. Coroniti 1990).

In our analysis we have considered an approximately aligned rotator, so that the striped wind region is so small to be dynamically unimportant and the assumption $B \sim \sin\theta$ remains valid even for $\theta \to \pi/2$ (the change of sign is superfluous, since B appears only squared in the dynamical equations). As mentioned in Sect. 2, in KL03 the opposite scenario is considered: the striped wind region is very large, such as to extend to intermediate latitudes affecting the overall field shape.

To understand what differences are to be expected, we have performed also a series of simulations with a magnetic field given as

$$B(r,\theta) = B_0 \frac{r_0}{r} \sin\theta \, \tanh[b(\pi/2 - \theta)], \qquad (10)$$

where B_0 is the same parameter defined in Sect. 2. in terms of σ, and b is a free numerical parameter defining the width of the
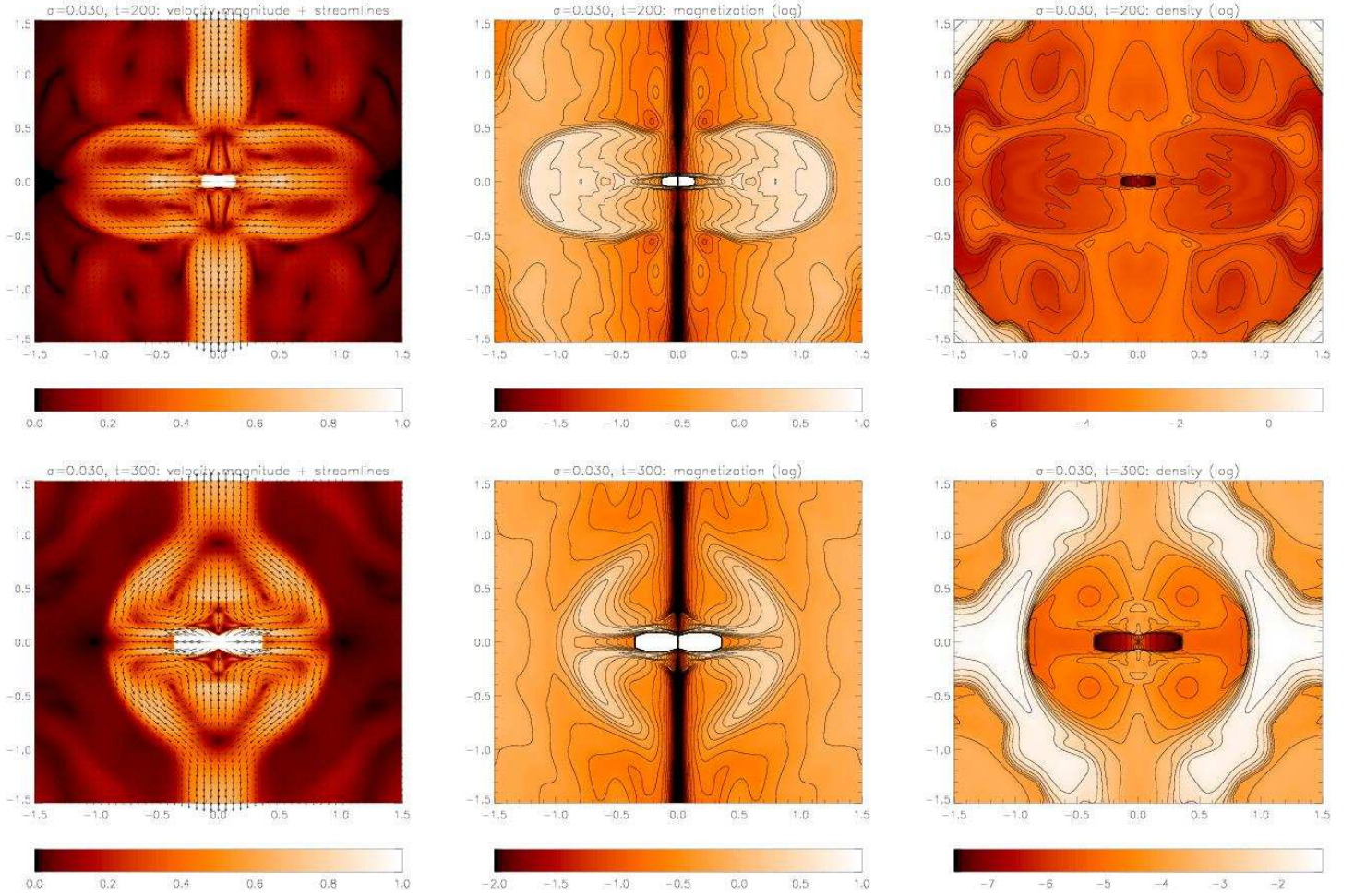
Fig. 7. The mechanism responsible for jet formation. Flow, magnetization and density maps are shown for the $\sigma = 0.03$ case at two different times: $t = 200$ (upper row) and $t = 300$ (lower row).
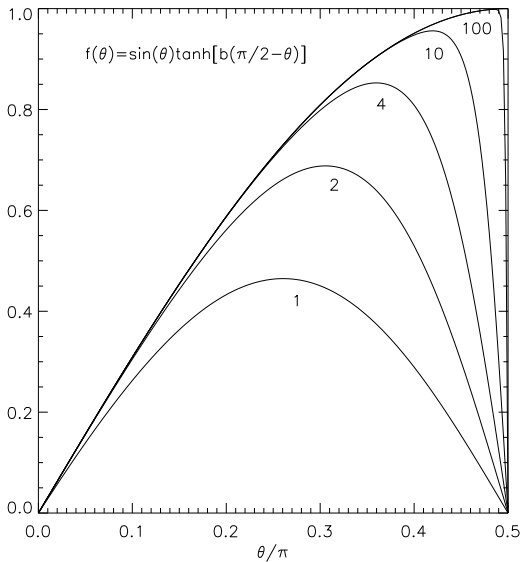

Fig. 8. The latitude dependence of the toroidal field, as defined by Eq.(10) (only the field above the equator is displayed). In this section the value $b = 10$ is employed.

striped wind region. In Fig. 8 we show the angular dependence of B for various values of b: $b \rightarrow \infty$ corresponds to the case discussed in all the previous sections, with $B \propto \sin\theta$, $b = 10$ is the case that will be considered in this section, while the field used in KL03 basically coincides with that in Eq. (10) for $b \approx 0.7$.

In Fig. 9 we show the same quantities as in Fig. 7 at time $t = 300$, again for the case $\sigma = 0.03$ but using the magnetic field of Eq. (10) with $b = 10$. The presence of an unmagnetized region around the equator (where the magnetic field was the highest in the previous cases) even as narrow as in the present case, is sufficient to change the picture completely. Now the TS is able to move further out at the equator. Around the narrow channel to which the equatorial outflow is confined, the magnetization grows rapidly and the hoop stresses are effective. As a consequence, collimation of a polar outflow still occurs, although the fraction of plasma now involved is less than when the magnetic field was non-vanishing at the equator. In particular (see Fig. 3 for comparison) the high speed funnel, instead of being completely diverted to the axis, splits into an equatorial outflow and in a backflow toward the axis. The corresponding
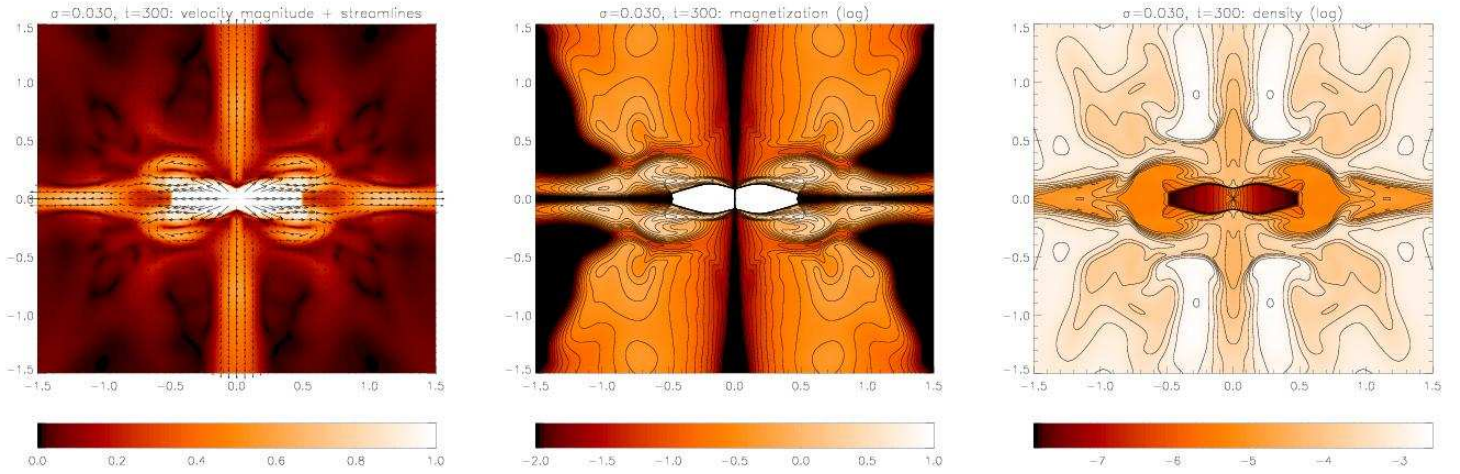
Fig. 9. Same quantities as in Fig. 7 at time $t = 300$, for a case with $\sigma = 0.03$ but with the field shape in the wind region given by Eq. (10).

streamlines now lie very close to the TS, and correspondingly also the polar jet forms much closer to the origin.

5. Conclusions

In this paper the structure and evolution of PWNe interacting with the surrounding SN ejecta has been analyzed by means of relativistic MHD axisymmetric simulations. Our main goal has been here the investigation of the mechanism originating the polar jets which are observed in X-rays in a growing number of PWNe.

The most recent and promising analytical studies (Bogovalov & Khangoulian 2002b, Lyubarsky 2002) start with the assumption that the pulsar wind is highly anisotropic, with a much larger energy flux at the equator than at the pole. Such a wind, interacting with the expanding SN ejecta produces a hot magnetized bubble with a torus-jet structure, as observed. The polar jet is originated by the magnetic hoop stresses in the PWN that, for high enough values of the wind magnetization parameter σ, divert part of the equatorial flow toward the axis, collimating and accelerating it. The first numerical RMHD simulations (Amato et al. 2003; KL03) confirm this scenario, and the simulated synchrotron emission map in the latter cited work strikingly resembles, at least qualitatively, the X-ray images of the Crab Nebula.

Here we have made an effort to improve on those preliminary simulations. The equatorial relativistic wind has a Lorentz factor as high as $\gamma = 100$, the magnetization parameter σ goes from 0.003 up to 0.1, which leads to magnetic fields in the PWN well beyond equipartition. The magnetic field shape assumed in the wind is that proper for an aligned or weakly oblique rotator, while in KL03 the assumed field is far from the $\sin\theta$ dependence, with a very broad region of low magnetization around the equator. The evolution is followed up to the beginning of the reverberation phase and comparison with previous models is made whenever possible.

The results show that the predicted self-similar evolution of the external PWN boundary is well reproduced at low magne-

tizations, and before reverberation effects begin. The expected elongation of the PWN due to magnetic pinching is also recovered, and we show how this effect increases in time and with σ. The elongation of the nebula appears to be independent on the wind anisotropy, measured in our model by the parameter α.

In the inner part of the PWN the termination shock assumes an oblate shape, as expected for an anisotropic wind energy flux. An equatorial supersonic flow is produced in a complex shock structure. At intermediate latitudes, where the TS is highly oblique, the downstream flow is still supersonic. The plasma moves along the front gradually focusing toward the equator. This pattern holds in hydrodynamical simulations as well, since it is due only to the wind flux anisotropy. The equatorial flow that is driven by this focusing mechanism is supersonic, with typical velocities of $v \approx 0.5 - 0.7c$, consistent with the values inferred for motion in the equatorial plane of the Crab Nebula (Hester et al. 2002).

When the wind magnetization is high enough ($\sigma \gtrsim 0.01$ in our simulations) the magnetic hoop stresses in the equatorial plane are so strong as to suppress completely this flow after a few termination shock radii. The plasma is then completely diverted toward the axis, where the magnetic compression finally drives a supersonic polar outflow with velocities that are once again in agreement with the values observed in the Crab and Vela PWNe ($v \approx 0.3 - 0.7c$, see Hester et al. 2002; Pavlov et al. 2003). At later times the interaction of the polar jets with the contact discontinuity density jump may cause additional effects. The flow circulates all the way along the CD from high latitudes down to the equatorial plane. Here, these large scale vortexes drag some dense material from the ejecta toward the origin, with the effect of confining the equatorial outflow to the very inner parts of the nebula. Notice that the circulation is the opposite (from the equator to the pole) in the hydro and low σ cases. The value of σ that distinguishes the two regimes that we call highly and lowly magnetizatized depends on the expansion velocity of the CD: for nebulae expanding at a larger rate we expect the transition to occur for higher wind magnetizations.

Finally, for the high σ cases, the flow pattern strongly depends on the Poynting flux distribution in the wind. In particular, if in a narrow region around the equator the magnetic field vanishes, an additional vortex appears in the circulation pattern. The equatorial supersonic flow is never suppressed completely: it reaches the CD and then it circulates back toward the axis. The polar jet is still present and drives a vortex circulating at higher latitudes in the opposite direction than the former.

In conclusion, axisymmetric relativistic MHD simulations of the interaction of pulsar winds with expanding SNRs are able to reproduce at least qualitatively most of the structures seen in X-ray images: the overall toroidal structure of the plerion, the supersonic motions in the equatorial plane and, if the wind magnetization is high enough, also the presence of polar jets with supersonic velocities. A more detailed study, with a larger sampling of the parameter space would be necessary for a quantitative comparison with the observations. An interesting perspective that the present study suggests is the inference of the wind magnetic field structure from direct comparison between simulated synchrotron maps and X-ray observations. Preliminary results are encouraging, although we prefer to leave quantitative comparisons as future work.

Some of the observed features are anyway impossible to reproduce within the present axisymmetric RMHD framework. Emission structures like knots and sprites might well be related to non-ideal effects, like magnetic reconnection and dissipation, that are non-trivial to deal with. Remaining within the RMHD approximation, a full 3-D setting would allow to deal with some non-axisymmetric instabilities that may play an important role in PWNe: let us mention as an example the kink instability, which is likely to be at the origin of the bending of the jet (observed in both the Crab and Vela nebulae). We also leave the study of these important physical processes as future work.

References

Amato E., Del Zanna L., Bucciantini N., 2003, in "Young Neutron Stars and their Environments" (IAU Symposium, 218, ASP Conference Proceedings), eds F. Camilo and B. M. Gaensler

Arons J., 2003, in "Young Neutron Stars and their Environments" (IAU Symposium, 218, ASP Conference Proceedings), eds F. Camilo and B. M. Gaensler

Begelman M.C.,Li Z.-Y. 1992, ApJ, 397, 187

Blondin J.M., Chevalier R.A., Frierson D.M., 2001, ApJ, 563, 806

Bogovalov S.V., 1999, A&A, 349, 101

Bogovalov S.V., Khangoulian D.V., 2002, Astronomy Letters, 28, 373

Bogovalov S.V., Khangoulian D.V., 2002, MNRAS, 336, 53

Bucciantini N., Blondin J.M., Del Zanna L., Amato E., 2003, A&A, 405, 617

Bucciantini N., Bandiera R., Blondin J.M., Amato E., Del Zanna L., 2004, A&A, *in press*

Coroniti F.V., 1990, ApJ, 349, 538

Del Zanna L., Bucciantini N., 2002, A&A, 390, 1177

Del Zanna L., Bucciantini N., Londrillo P., 2003, A&A, 400, 397

Emmering R.T., Chevalier R.A., 1987, ApJ, 321, 334

Gaensler B.M., Pivovaroff M.J., Garmire G.P., 2001, ApJ, 556, 380

Gaensler B.M., Arons J., Kaspi V.M., Pivovaroff M.J., Kawai N., Tamura K., 2002, ApJ, 569, 878

Gallant, Y.A., Arons J., 1994, ApJ, 435, 230

Helfand D.J., Gotthelf E.V., Halpern J.P., 2001, ApJ, 556, 107

Hester J.J. et al., 1995, ApJ, 448, 240

Hester J.J. et al., 2002, ApJ, 577, L49

Kennel C.F., Coroniti F.V., 1984, ApJ, 283, 694

Khangoulian D.V., Bogovalov S.V., 2003, Astronomy Letters, 29, 495

Komissarov S.S., Lyubarsky Y.E., 2003, MNRAS, 344, L93

Lyubarsky Y.E., 2002, MNRAS, 329, L34

Lyubarsky Y.E., Eichler D., 2001, ApJ, 562, 494

Lu F.J., Wang Q.D., Aschenbach B., Durouchoux P., Song L.M., 2002, ApJ, 568, 49L

Michel F.C., 1973, ApJ, 180, 133

Pavlov G.G., Teter M.A., Kargaltsev, O., Sanwal D., 2003, ApJ, 591, 1157

van der Swaluw E., Achterberg A., Gallant Y.A., Toth G., 2001, A&A, 380, 309

van der Swaluw E., 2003, A&A, 404, 939

Vlahakis N., 2004, ApJ, 600, 324

Weisskopf M.C. et al., 2000, ApJ, 536, L81